Neurobiology of Disease 124 (2019) 218–229

Contents lists available at ScienceDirect

Neurobiology of Disease

journal homepage: www.elsevier.com/locate/ynbdi

SIL1 deficiency causes degenerative changes of peripheral nerves and neuromuscular junctions in fish, mice and human

Vietxuan Phan[a], Dan Cox[b], Silvia Cipriani[b,c], Sally Spendiff[d,m], Stephan Buchkremer[e], Emily O'Connor[b], Rita Horvath[f], Hans Hilmar Goebel[g], Denisa Hathazi[a], Hanns Lochmüller[d,h,m], Tatjana Straka[i,j,k], Rüdiger Rudolf[i,j,k], Joachim Weis[e], Andreas Roos[a,e,l,*]

[a] Leibniz-Institut für Analytische Wissenschaften, ISAS, e.V. Dortmund, 44227, Dortmund, Germany
[b] MRC Centre for Neuromuscular Diseases, Institute of Genetic Medicine, Newcastle University, Newcastle upon Tyne, UK
[c] Department of Neuromotor and Biomedical Sciences, Pathology Unit, University of Bologna, Bologna, Italy
[d] Children's Hospital of Eastern Ontario Research Institute, University of Ottawa, Ottawa, Canada
[e] Institute of Neuropathology, University Hospital RWTH Aachen, Aachen, 52074, Germany
[f] Department of Clinical Neurosciences, University of Cambridge, Cambridge Biomedical Campus, Cambridge CB2 0QQ, UK
[g] Department of Neuropathology, Charité Berlin, Germany
[h] Department of Neuropediatrics and Muscle Disorders, Medical Center, University of Freiburg, Faculty of Medicine, Freiburg, Germany
[i] Institute of Molecular and Cell Biology, Mannheim University of Applied Sciences, Mannheim, Germany
[j] Interdisciplinary Center for Neurosciences, Heidelberg University, Heidelberg, Germany
[k] Institute of Toxicology and Genetics, Karlsruhe Institute of Technology, Eggenstein-Leopoldshafen, Germany
[l] Pediatric Neurology, University Childrens Hospital, University of Duisburg-Essen, Faculty of Medicine, Essen, Germany
[m] Division of Neurology, Department of Medicine, The Ottawa Hospital, Ottawa, Canada

ARTICLE INFO

Keywords:
SIL1
Marinesco-Sjögren syndrome
Woozy
PNS pathology
Neuromuscular junction

ABSTRACT

Background: Marinesco-Sjögren Syndrome (MSS) is a rare neuromuscular condition caused by recessive mutations in the *SIL1* gene resulting in the absence of functional SIL1 protein, a co-chaperone for the major ER chaperone, BiP. As BiP is decisive for proper protein processing, loss of SIL1 results in the accumulation of misshaped proteins. This accumulation likely damages and destroys cells in vulnerable tissues, leading to congenital cataracts, cerebellar ataxia, vacuolar myopathy and other MSS phenotypes. Whether the peripheral nervous system (PNS) is affected in MSS has not been conclusively shown.

Methods: To study PNS vulnerability in MSS, intramuscular nerves fibres from MSS patients and from SIL1-deficient mice (*woozy*) as well as sciatic nerves and neuromuscular junctions (NMJ) from these mice have been investigated *via* transmission electron microscopic and immunofluorescence studies accompanied by transcript studies and unbiased proteomic profiling. In addition, PNS and NMJ integrity were analyzed *via* immunofluorescence studies in an MSS-zebrafish model which has been generated for that purpose.

Results: Electron microscopy revealed morphological changes indicative of impaired autophagy and mitochondrial maintenance in distal axons and in Schwann cells. Moreover, changes of the morphology of NMJs as well as of transcripts encoding proteins important for NMJ function were detected in *woozy* mice. These findings were in line with a grossly abnormal structure of NMJs in SIL1-deficient zebrafish embryos. Proteome profiling of sciatic nerve specimens from *woozy* mice revealed altered levels of proteins implicated in neuronal

Abbreviations: A1AT5A, alpha-1-antitrypsin 1–5; AChR, acetylcholine receptor; ALS, Amyotrophic Lateral Sclerosis; ANOVA, analysis of variance; ATOX1, copper transport protein; CCFDN, congenital cataracts, facial dysmorphism and peripheral neuropathy; CLIC6, chloride intracellular channel protein 6; COL1A1 and COL1A2, collagen alpha 1 type 1 and 2; ER, endoplasmic reticulum; FASP, filter-aided sample preparation; FDR, false discovery rate; GRP78, BiP: 78 kDa glucose-regulated protein; HCD, high collision induced dissociation; HSP, heat shock protein; GO, gene ontology; MSS, Marinesco-Sjögren Syndrome; MOs, morpholino oligonucleotides; MUG1, murinoglobulin-1; NCAM, neural cell adhesion molecule; NMJs, neuromuscular junctions; NTC, no-template control; PNPH, purine nucleoside phosphorylase; PNS, peripheral nervous system; POSTN, periostin; PYC, pyruvate carboxylase; ROI, region of interest; RT, room temperature; SA3K, serine protease inhibitor A3K; TYB4, thymosin beta-4; UPR, unfolded protein response

* Corresponding author at: Leibniz-Institut für Analytische Wissenschaften, ISAS, e.V., Otto-Hahn-Str. 6b, 44227 Dortmund, Germany.
E-mail addresses: vietxuan.phan@isas.de (V. Phan), dan.cox@nnewcastle.ac.uk (D. Cox), silvia.cipriani5@studio.unibo.it (S. Cipriani), SSpendiff@cheo.on.ca (S. Spendiff), sbuchkremer@ukacchen.de (S. Buchkremer), emily.o'connor@newcastle.ac.uk (E. O'Connor), rita.horvath@doctors.org.uk (R. Horvath), hans-hilmar.goebel@charite.de (H.H. Goebel), denisa.hathazi@isas.de (D. Hathazi), t.straka@hs-mannheim.de (T. Straka), r.rudolf@hs-mannheim.de (R. Rudolf), jweis@ukaachen.de (J. Weis), andreas.roos@isas.de (A. Roos).

https://doi.org/10.1016/j.nbd.2018.11.019
Received 1 June 2018; Received in revised form 21 October 2018; Accepted 19 November 2018
Available online 20 November 2018

maintenance suggesting the activation of compensatory mechanisms.
Conclusion: Taken together, our combined data expand the spectrum of tissues affected by SIL1-loss and suggest that impaired neuromuscular transmission might be part of MSS pathophysiology.

1. Background

Marinesco-Sjögren syndrome (MSS; MIM:248800) is a rare autosomal recessive disorder that affects multiple organ systems. Common symptoms of MSS are congenital cataracts, cerebellar ataxia, hypotonia, progressive muscle weakness, and delayed psychomotor development (Goto et al., 2014; Herva et al., 1987; Sjogren, 1950; Superneau et al., 1987). The disease affects males and females equally; however, the exact incidence of the disorder in the general population is unknown. MSS is often caused by mutations of the *SIL1* gene which locates on the long arm of chromosome 5 (5q31.2) (Anttonen et al., 2005; Senderek et al., 2005). SIL1, an adenine nucleotide exchange factor, binds to the 78 kDa glucose-regulated protein (GRP78; BiP) and thereby regulates its ATPase cycle. BiP belongs to the heat shock protein (HSP) 70 chaperone family and plays a key role in protein quality control within the endoplasmic reticulum (ER) (Chung et al., 2002; Zoghbi, 2005). Loss of functional SIL1 results in the build-up of misfolded proteins in the ER and thus to activation of the unfolded protein response (UPR) and likely damages cells in many tissues, leading to congenital or infantile cataracts, Purkinje cell degeneration and ataxia, progressive vacuolar myopathy and other phenotypes such as MSS complicated by Dandy-Walker syndrome (Gai et al., 2016), by spastic paraplegia (Noreau et al., 2015) or by motor neuronopathy and bradykinetic movement disorder (Byrne et al., 2015). Overall, this phenotype highlights an important role of SIL1 in neuronal function and maintenance. In *woozy* mice, loss of functional SIL1 results in ER-stress, UPR activation and Purkinje cell degeneration and vacuolar myopathy with signs of altered autophagy and typical alterations of the myonuclear envelope, indicating that the woozy mouse is a suitable phenocopy of the human disease (Inaguma et al., 2014; Roos et al., 2014; Zhao et al., 2010; Zhao et al., 2005).

In the nervous system, ER stress has been identified as a key process in multiple neurodegenerative conditions such as Alzheimer's and Parkinson's disease, Amyotrophic Lateral Sclerosis (ALS) and prion diseases (Doyle et al., 2011; Stetler et al., 2010). In this context, it is important to note that apart from the above described MSS phenotype, a prominent role of SIL1 in maintaining integrity and function of the nervous system is suggested by the following observations: (i) SIL1 has been described as a disease-modifying protein in ALS and Alzheimer's disease, respectively (Filézac de L'Etang et al., 2015; Liu et al., 2016), (ii) *in vitro* overexpression of SIL1 resulted in elevation of a variety of proteins with neuroprotective functions (Labisch et al., 2017), (iii) *in vitro* depletion of SIL1 affects several proteins important for neuronal function (Roos et al., 2016) and (iv) morphological studies of Sil1-mutant mice revealed pathological alterations of nerve terminals and neuromuscular junctions along with signs of neurogenic muscular atrophy (Filézac de L'Etang et al., 2015). Although Horvers and co-workers found no clear evidence of peripheral neuropathy in their cohort of four Dutch MSS patients with proven *SIL1* mutations (Horvers et al., 2013); still, the evidence discussed above suggests a vulnerability of the PNS against loss of functional SIL1. However, so far there is no dedicated study focusing on the effect of SIL1 deficiency on peripheral nerves and neuromuscular junctions (NMJs). To systematically address this question, we investigated intramuscular nerve fascicles in MSS-patients and *woozy* mice as well as the sciatic nerves of these mice by transmission electron microscopy. Moreover, proteomic profiling of the murine sciatic nerve was performed to obtain insights into the biochemical consequences of loss of the SIL1 protein in the PNS. Finally, NMJs were systematically studied by immunofluorescence in *Sil1*-mutant and wildtype mice as well as in an MSS-zebrafish model.

2. Materials and methods

2.1. Electron microscopy

Ultrathin sections of archived glutaraldehyde-fixed, resin-embedded *M. quadriceps* biopsies obtained from two MSS-patients with proven *SIL1* mutations (Senderek et al., 2005; Krieger et al., 2013) were examined. In addition, sciatic nerve specimens derived from *woozy* (Zhao et al., 2005) (3 animals aged 16 weeks and 3 animals aged 26 weeks) and wildtype mice (3 animals aged 16 weeks and 3 animals aged 26 weeks) were fixed in 3.9% buffered glutaraldehyde. Samples were osmicated in 1% phosphate-buffered osmium tetroxide, dehydrated and embedded in epoxy resin. Ultrathin sections (100 nm) of transversely and longitudinally embedded nerve fascicles were contrasted with uranyl acetate and lead citrate. EM images were obtained using a CM10 transmission electron microscope (Philips, Amsterdam, The Netherlands).

2.2. Proteomic profiling

2.2.1. Tissue lysis and carbamidomethylation

Sciatic nerves derived from three *woozy* and three wild-type animals were used for comparative proteome profiling utilizing a label-free approach. Each sample was ground and lysed in 0.5 mL of 50 mM Tris-HCl (pH 7.8) buffer containing 150 mM NaCl, 1% SDS and Complete Mini. Afterwards, extracts were centrifuged at 13,500 ×*g* for 30 min at 4 °C and protein lysate was collected. The protein concentration of each sample was determined by BCA assay according to the manufacturer's protocol. Then, cysteines of the proteins were reduced by addition of 10 mM DTT at 56 °C for 30 min, followed by alkylation of free thiol groups with 30 mM IAA at room temperature (RT) in the dark for 30 min.

2.2.2. Sample preparation and trypsin digestion

Sample preparation and proteolysis were performed using filter-aided sample preparation (FASP). Briefly, 100 µg of protein was diluted 10-fold with freshly prepared 8 M urea/100 mM Tris-HCl (pH 8.5) buffer and placed on a centrifugal device Nanosep 30 kDa Omega (Life Science). The device was centrifuged at 13,800 *g* at RT for 20 min for all centrifugation steps. First, to eliminate residual SDS, three washing steps were carried out with 100 µL of 8 M urea/100 mM Tris-HCl (pH 8.5). Then, for buffer exchange, the device was washed thrice with 100 µL of 50 mM NH_4HCO_3 (pH 7.8). Next, 100 µL of proteolysis buffer comprising of trypsin (Promega) (1:25 w/w, protease to substrate), 0.2 M GuHCl and 2 mM $CaCl_2$ in 50 mM NH_4HCO_3 (pH 7.8), was added to the device and incubated at 37 °C for 14 h. Afterwards, the generated tryptic peptides were recovered by centrifugation with 50 µL of 50 mM NH_4HCO_3 followed by 50 µL of ultra-pure water. Finally, peptides were acidified by addition of 10% TFA (v/v) and digests were quality-controlled in a reversed-phase HPLC.

2.2.3. LC-MS/MS analysis

Replicates were measured using an UltiMate 3000 nano RSLC System coupled to a Lumos Dionex Mass Spectrometer (both from Thermo Scientific). Peptides were preconcentrated on a 100 µm × 2 cm, C18, 5 µm, 100 Å trapping column for 10 min using 0.1% TFA (v/v) at a flow rate of 20 µL/min followed by separation on 75 µm × 50 cm, C18, 2 µm, 100 Å main column (both from Acclaim Pepmap, Thermo Scientific) with a 120 min LC gradient ranging from 3 to 35% of 84% ACN, 0.1% FA (v/v) at a flow rate of 250 nL/min. MS

survey scans were acquired in the Orbitrap from *m/z* 300 to 1500 at a resolution of 120,000 using the ambient air (protonated (Si(CH3)2O)6) ion at *m/z* 445.12002 as lock mass (Schlosser and Volkmer, 2003). The most intense signals were subjected to high collision induced dissociation (HCD), and the detection was archived in the ion trap, taking into account a dynamic exclusion of 30 s. HCD spectra were acquired with a normalized collision energy of 30% and an activation time of 10 ms. AGC target values were set to 2×10^6 for Orbitrap MS and 2×10^4 for ion trap MSn scans. Maximum injection times were set to 50 ms and 300 ms for both full MS and MSn scans, respectively.

2.2.4. Label free data analysis

Data analysis of the acquired label free quantitative MS data was performed using the Progenesis Qi software from Nonlinear Dynamics (Newcastle upon Tyne, U.K.) in which alignment of MS raw data was conducted by automatically selecting one of the LC-MS files as reference. After peak picking, only features within retention time and m/z windows from 0 to 120 min and 300–1500 *m/z*, with charge states +2, +3, and +4 were considered for peptide statistics and analysis of variance (ANOVA). MS/MS spectra were exported in an mgf file as peak lists.

The mgf peak lists were searched against a concatenated target/decoy version of the mouse Uniprot database (downloaded in July 2015, containing 16,716 target sequences) using Mascot 2.4.0 (Matrix Science), X! TANDEM Vengeance (2015.12.15.2) and MS-GF+ Beta (v10282) (12/19/2014) with the help of searchGUI 2.8.4. Trypsin with a maximum of two missed cleavages was selected as enzyme. Carbamidomethylation of cysteine was set as fixed and oxidation of methionine was selected as variable modification. MS and MS/MS tolerances were set to 10 ppm and 0.5 Da, respectively.

PeptideShaker software 1.10.2 was used for interpretation of peptide and protein identifications from searchGUI and Mascot. Combined search results were filtered at a false discovery rate (FDR) of 1% on the protein level and exported using the advanced PeptideShaker features that allow direct re-import of the quality-controlled data into Progenesis Qi. Peptide sequences containing oxidized methionines were excluded for further analysis. Only proteins that were quantified with unique peptides were exported. Then, for each protein, the average of the normalized abundances (obtained from Progenesis Qi) from the replicate analyses was calculated to determine the ratios between the woozy and the wildtype mice. Only proteins which were (i) commonly quantified in all the replicates with (ii) at least a unique peptide, (iii) an ANOVA *p*-value of < 0.05 (Progenesis Qi) and (iv) an average log2 ratio of which protein that was either higher than the up-regulated cut-off or lower than the down-regulated cut-off was considered as regulated. The cut-off values were determined based on the 2× standard deviation and the normal distribution from all identified protein's log2 ratio in which the bell curve is symmetric around the mean. Therefore, an average log2 ratio of a protein which < -1.02 or > 1.05 (corresponding to ~2.09-fold regulation; log2 ratios of 1.01) for comparative global profile were considered as regulated.

2.3. Morphological studies of neuromuscular junctions in woozy mice

Immunofluorescence staining of 100 µm-thick free-floating longitudinal sections of *Extensor Digitorum Longus* muscles were done as previously described (Khan et al., 2016). Briefly, muscles were incubated in 1× PBS/0.5% Tween-20 with 10 µg/mL Heparin (1× PTwH) for 24 h at room temperature. Then, muscles were transferred to 1× PBS/1× PTwH/0.5% Triton X-100/10% (vol/vol) DMSO/6% (vol/vol) BSA (1× BnP) at room temperature for 5 days. Followed by incubation with Bungarotoxin 647 (Invitrogen/B35450) in 1 × BnP solution for 5 d at 37 °C. After the staining, muscles were washed with PTwH solution for 5d at RT before imaging. Muscles were placed in a 35 mm glass bottom dish and imaged with an inverted Leica SP2 (Leica Microsystems, Mannheim, Germany) confocal microscope equipped with a HC PL APO 20×/0.75 IMM CORR UV objective. 3D stacks were taken at 8-bit, 1024 × 1024 pixel resolution, and 400 Hz scan frequency. Images were electronically processed using ImageJ software (NIH, Bethesda, MD). NMJ area was determined using the region of interest (ROI) upon thresholding at 30–255 greyscale values.

2.4. Transcript studies in Sil1-mutant and wildtype mice

To further examine the integrity of the NMJ gene expression investigations were performed for targets previously shown to be involved in NMJ structure (Aare et al., 2016). RNA was extracted from the muscle of 26-week-old mice. TRIzol Reagent (Ambion), 0.1 mL per 50–100 mg of muscle weight, was added to each sample. The samples were homogenised on ice using a TissueRuptor (Qiagen) and incubated for 5 min at room temperature before centrifuging for 10 min at 12,000 g (4 °C). 0.2 mL of Chloroform per 1 mL of Trizol was added to the cleared homogenate solution and the sample vigorously shaken by hand for 15 s. Samples were incubated for 3 min at room temperature, centrifuged for 15 min at 12,000 g (4 °C), and the RNA in the aqueous phase transferred to a new tube. 0.5 mL per 1 mL of Trizol of isopropyl alcohol was added to each sample which was again shaken by hand before incubation at room temperature for 10 min. Samples were centrifuged for 15 min to obtain the RNA pellet, which was then washed in 75% ETOH and centrifuged for 5 min. The supernatant was removed, and the pellet dried in a heat block at 55–60 °C.The RNA was re-suspended in RNAase-free-water (Ambion)and incubated at 55–60 °C for 10 min. Sample purity (A_{260}/A_{280} ratio) and concentration (µg/µl) were assessed using a Nanodrop2000 (ThermoFisher).

DNAase treatment and reverse transcription was performed according to manufacturer's instructions using the DNA-free™ DNA Removal Kit (ThermoFisher) and the High-Capacity cDNA Reverse Transcription Kit (ThermoFisher) respectively. Samples were stored at −20 °C until use.

Real-time PCR (qPCR) was performed on a BioRad CFX96 using

Table 1
Oligonucleotides used for the transcription studies.

Gene	Forward Sequence	Reverse Sequence	Annealing temp (°C)	NCBI Ref
AChRγ (Aare et al., 2016)	GACCAACCTCATCTCCCTGA	GAGAGCCACCTCGAAGACAC	60	NM_009604.3
NCAM (Aare et al., 2016)	AAGGGGAAGGCACTGAATTT	TCTCCTGCCACTTGACACAG	60	NM_001081445.1
AchRα (Aare et al., 2016)	TCCCTTCGATGAGCAGAACT	GGGCAGCAGGAGTAGAACAC	60	NM_007389.5
NGF (Aare et al., 2016)	GCAGTGAGGTGCATAGCGTA	CTGTGTCAAGGGAATGCTGA	60	NM_001112698.2
TATA BOX BP (Aare et al., 2016)	TGCCCAGCATCACTATTTCA	CCGTAAGGCATCATTGGACT	60	NM_013684.3
AchRε (Aare et al., 2016)	GCAGCTTTTACCGAGAATGG	CGTCAGTTTCTCCAGGACC	60	NC_000077.6
MuSK (Aare et al., 2016)	TTCAGCGGGACTGAGAAACT	TGTCTTCCACGCTCAGAATG	61.5	NM_001037127.2
BDNF (Aare et al., 2016)	TAATGCAGCATGATGGGAAA	TCACAGTGAAAGCACCTTGC	60	NM_001048139.1
NGF (Aare et al., 2016)	GCAGTGAGGTGCATAGCGTA	CTGTGTCAAGGGAATGCTGA	60	NM_001112698.2
NTRK2 (Roy et al., 2010)	CGGCACATAAATTTCACACG	GTGAGGTTAGGAGCAGCCAG	63.9	NM 008745.2
NTRK3 (Roy et al., 2010)	AAGTAACCGGCTCACCACAC	GATGCAGTAAAGGCTCTGGC	63.9	NM_182809.2
P75 (Roy et al., 2010)	CAACCAGACCGTGTGTGAAC	GAGAACACGAGTCCTGAGCC	63.9	NM 033217.3

Power SYBR Green Master Mix (ThermoFisher). For each gene examined, a temperature gradient and dilution calibration curve were performed to determine optimum conditions for the primer pair (Table 1) and check the reaction efficiency. A master mix composed of 10 µL of SYBR Green, 6 µL of DEPC-H_2O, 1 µL of forward and reverse primer (Table 1) was added to 2 µL of cDNA. Samples were run in triplicate along with a no-template control (NTC), with only wells that were at least 3 Cq cycles away from the NTC being used for analysis. Data was analyzed using the ΔΔCq method.

2.5. Generation of a MSS-zebrafish model and studies of NMJ integrity and myelination

To examine NMJ integrity and myelination, knockdowns were performed in zygotes of the Golden (slc24a5b1/+) *Danio rerio* strain (ZIRC, OR, USA). Zebrafish embryos and larvae were raised and staged according to standard procedures (Kimmel et al., 1995).

Antisense morpholino oligonucleotides (MOs) were purchased from Gene Tools (Pilomath, OR). We obtained a previously published (Kawahara and Hayashi, 2016) *Sil1* splice-blocking MO directed against the splice acceptor site of exon 2 (5′-GGTGACTGTGTAAACAGAACAA ATC-3′). The Gene Tools standard control-MO targeting a human β-hemoglobin gene (5′-CCTCTTACCTCAGTTACAATTTATA-3′) was used as a negative control for the effects of MO injection. Zygotes were injected with 6 ng of either *Sil1* MO or control-MO following standard protocols.

Bright field microscopy images of larvae were captured using a Leica dissection stereomicroscope equipped with a Leica digital camera (model DFC 420C). For immunofluorescent staining of whole mount zebrafish, 5-day post fertilization zebrafish embryos were dechorionated using Pronase E (Sigma Aldrich) and euthanized by anesthetic overdose. Whole mount staining was performed as described previously (Müller et al., 2010), utilizing a mouse anti-SV2 antibody to visualize the motor neurons (1:200, Developmental Studies Hybridoma Bank) and Alexa Fluor 594-α-bungarotoxin conjugate to visualize acetylcholine receptors (1:1000, Thermo Fisher). A Claudin K antibody (1:200) was used for myelin-staining. *Z*-stack images encompassing the entire zebrafish tail were obtained using a 20× air objective on a Nikon A1R confocal microscope.

3. Results

3.1. Electron microscopy

EM of intramuscular nerves found in quadriceps muscles of MSS patients revealed accumulations of membranous autophagic/mitophagic material as well as spheroid-like accumulations of cytoskeletal elements and of organelles associated with a thinning of the myelin sheaths in axons; a similar buildup of autophagic material was also present in Schwann cells of myelinated and unmyelinated nerve fibres (Fig. 1).

Similar alterations were found in quadriceps intramuscular nerves of 26-week-old (Fig. 2) and in sciatic nerves of 16 and 26-week-old *woozy* mice (Figs. 3, 4) but not in nerves derived from respective

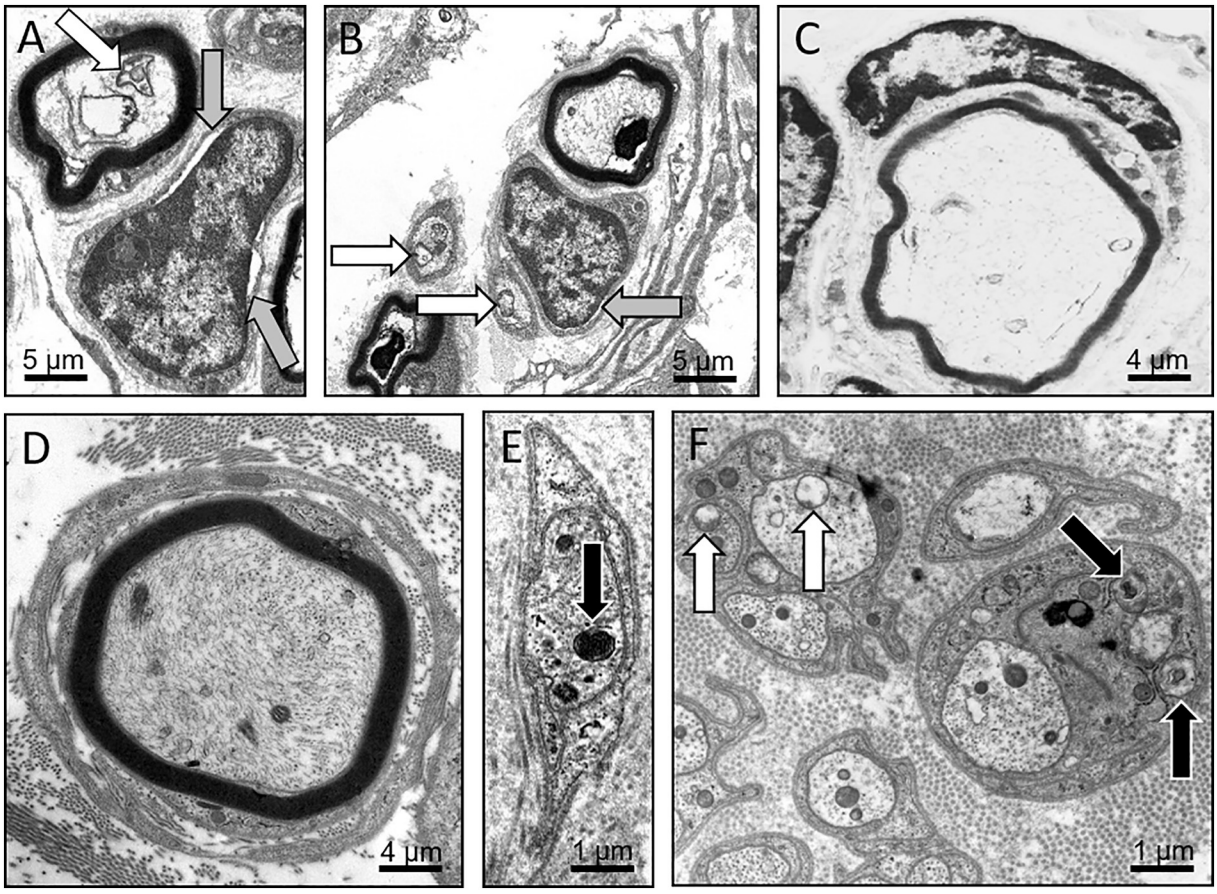

Fig. 1. EM of intramuscular nerve fibres in MSS patient skeletal muscle. (A, B) Membranous material and swollen/degenerated mitochondria (white arrows) and nuclear envelope widening combined with chromatin condensation in Schwann cells (grey arrows). (C, D) Spheroid-like accumulation of cytoskeletal elements and of organelles associated with a thinning of the myelin sheaths. The nerve fibre depicted in (D) is surrounded by a surplus Schwann cell process. (E) Autophagic material (black arrow) in an unmyelinated axon. (F) Autophagic material (black arrows) in the cytoplasm of a Schwann cell; swollen mitochondria in unmyelinated axons (white arrows).

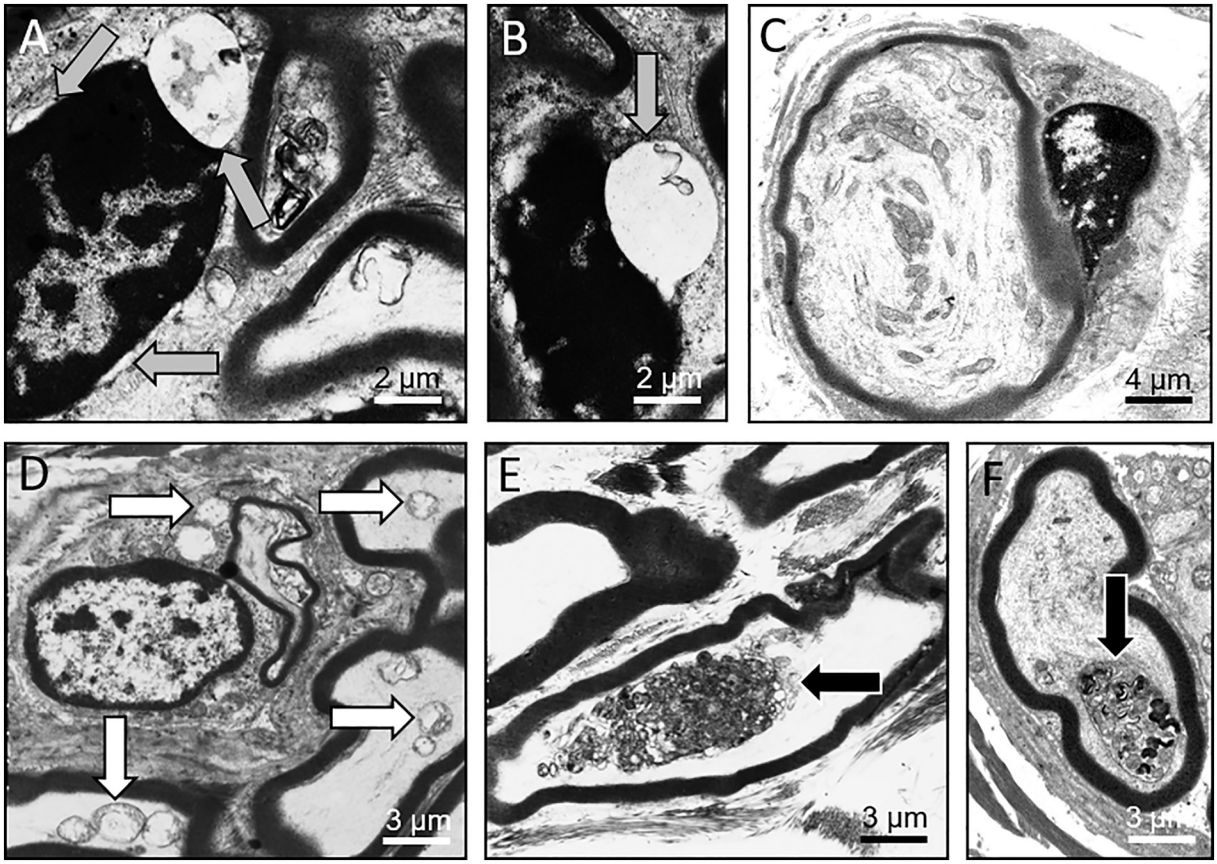

Fig. 2. Ultrastructural alterations in 26-week-old woozy mouse intramuscular (quadriceps muscle) nerve fascicles. (A, B) Focal widening (grey arrows) of the nuclear envelope of Schwann cells. (C) Spheroid-like swelling of a myelinated nerve fibre due to intraaxonal accumulation of cytoskeletal elements and organelles. (D) Swollen intraaxonal mitochondria (white arrows). (E, F) Large accumulations of granular and membranous autophagic material in the axons and/or in the adaxonal Schwann cell cytoplasm (black arrows).

wildtype littermates (data not shown). In addition, prominent widenings of the space between the inner and the outer leaflets of the nuclear envelope in Schwann cells was observed in MSS-patients and these mice; these vacuolar structures often contained granular or membranous electron-dense material (Figs. 1, 2). Aberrant, often widened endoplasmic reticulum structures were observed in both human patient and *woozy* mouse Schwann cells (Figs. 1–4). Axons with disproportionately thin myelin sheaths could be occasionally found in both, MSS-patients and *woozy* mice (Figs. 1–3). Notably, even though the deposits of electron dense autophagic material became more prominent in myelinated and non-myelinated axons (11% in 16-week-old and 21% in 26-week-old mutant animals on average) as well as in Schwann cells in 26-week-old animals (10% in 16-week-old and 16% in 26-week-old mutant animals on average) (Figs. 3, 4), the mild perturbations of myelination did not increase with age. Perturbations of the nuclear envelope are detectable in 7% of Schwann cell nuclei on average. The mitochondrial changes occurred with 12% on average in the PNS of 16-week-old mutant mice and with 26% on average in the PNS of 26-week-old *woozy* animals.

3.2. SIL1 deficiency perturbs integrity of neuromuscular junctions in woozy mice and MSS zebrafish

Prompted by our previous observation that in *woozy* mice, integrity of the NMJs is disturbed and that this is associated with signs of neurogenic atrophy of muscle fibres (Filézac de L'Etang et al., 2015), we investigated NMJs in *extensor digitorum longus* muscles from 26-week-old *woozy* and wild-type mice and in a MSS-zebrafish model. Morphological investigation of a total of 100 NMJs stained with bungarotoxin revealed a statistically significant reduction in the size of NMJs in the *woozy* animals (Fig. 5A, B). Moreover, in mutant mice, the fluorescence intensity of α-bungarotoxin appeared weaker thus suggesting reduced presence of AChR compared to wildtype NMJs (Fig. 5A). Immunofluorescence of NMJs in zebrafish Sil1 morphants illustrated a disruption of synapse formation along the vertical myosepta with a striking disorganization of presynaptic branching across the muscle fibres of the myotomes compared to those observed in control fish (Fig. 6A). Further studies of myelinating Schwann cells using a Claudin K antibody did not show significant differences between control-morpholino and Sil1-morpholino injected fish (Fig. 6B).

3.3. Gene expression analysis of de-innervation and re-innervation

The gene expression analysis of de-innervation and re-innervation markers, performed on *Sil1* mutant and wildtype mice, revealed significant changes supporting the concept of perturbed NMJ integrity and function: among the investigated de-innervation markers, transcripts of *AChRγ* and *N-CAM* were respectively 36.05-fold and 3.58-fold higher in mutant than in wildtype animals whereas the other transcript marker (*AChRα*, *AChRε*, *MuSK*) values were not statistically significant changed in abundances. Re-innervation transcript markers (*BDNF*, *NGF*, *NTRK2*, *NTRK*, *p75*) did not show significant changes in transcript abundances (Fig. 5D).

3.4. SIL1-mutant sciatic nerves display changes in protein abundances

Proteomics is a powerful tool for the unbiased investigation of pathophysiological processes (Burkhart et al., 2014; Roos et al., n.d.).

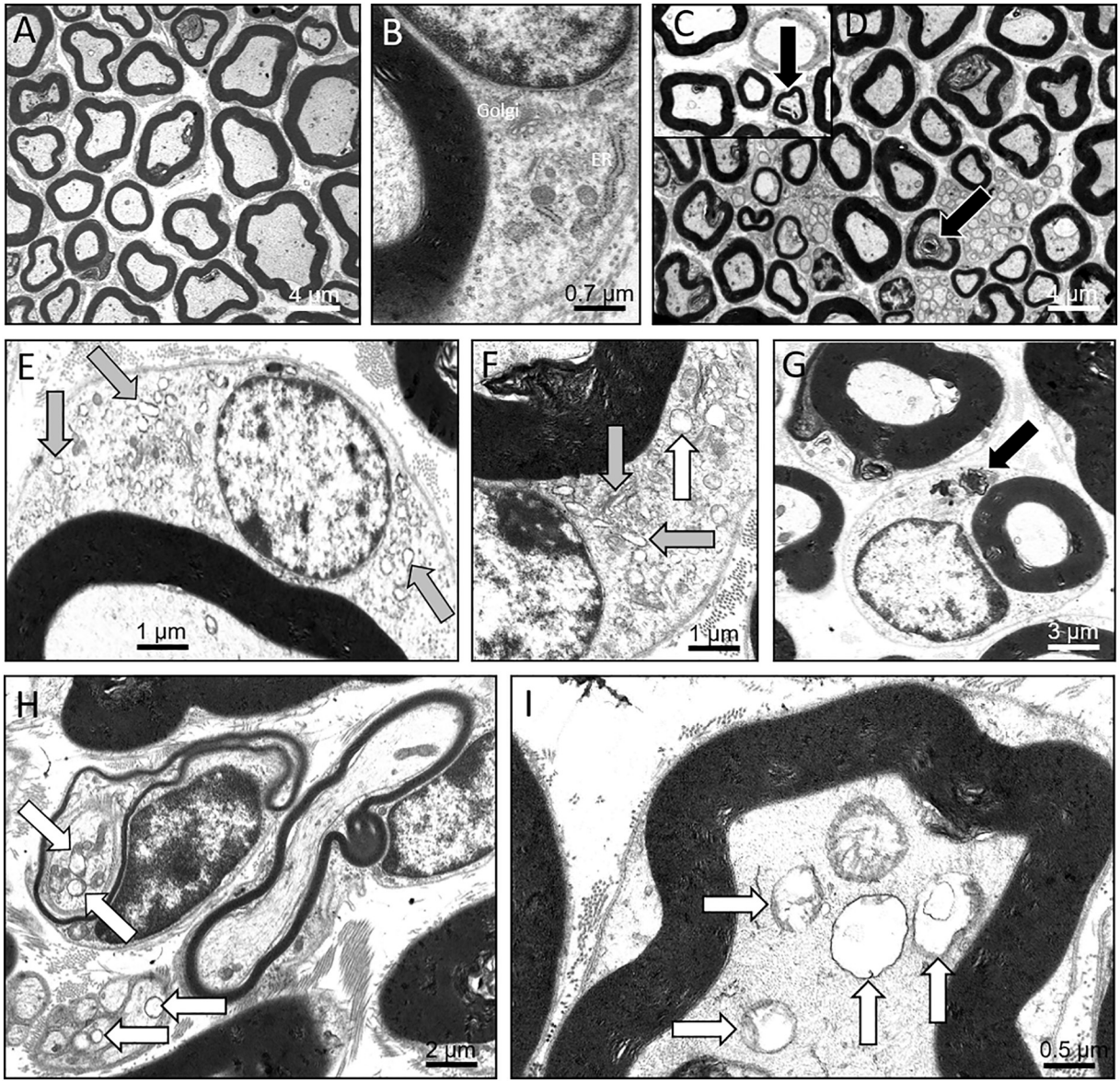

Fig. 3. EM of 16-week-old control and woozy mouse sciatic nerves. (A, B) Normal control nerve fibres. (C, D) Membranous cytoplasmic bodies (black arrows) in woozy mouse nerve fibres. (E, F) Prominent ER/Golgi structures in the cytoplasms of Schwann cells of myelinated fibres (grey arrows) and degenerating mitochondrion (white arrow). G Autophagic vacuole in a Schwann cell (black arrow). (H) Disproportional thin myelinated axons and (H, I) prominent, swollen intraaxonal mitochondria (white arrows).

Here, we compared *Sil1*-mutant and wildtype sciatic nerves using quantitative mass spectrometry. We found that 1.22% of the quantified proteins (20 out of 1632) were differentially expressed upon loss of functional SIL1 in this tissue: 15 (0.92%) of these proteins were upregulated and 5 (0.3%) downregulated (Fig. 7A–C). The affected proteins are located to the cytoplasm, cellular membranes and the extracellular space (Fig. 7D). For an overview on the regulated proteins and proposed functions, see supplemental table 1. To provide insight into SIL1 neuronal cytopathology, the spectrum of affected proteins was analyzed for enriched gene ontology (GO) terms using STRING (Franceschini et al., 2013) (Suppl. Fig. 1).

4. Discussion

4.1. PNS is vulnerable against the loss of SIL1

Recessive SIL1 mutations cause MSS in human patients and the *woozy* phenotype in mice (Roos et al., 2014; Zhao et al., 2005; Krieger et al., 2013), both with degeneration of Purkinje cells and ataxia. Some MSS patients present with additional Dandy-Walker syndrome (Gai et al., 2016), spastic paraplegia (Noreau et al., 2015) or motor neuronopathy associated with bradykinetic movement disorder (Byrne et al., 2015). Moreover, *Sil1* knock down in zebrafish by two different antisense oligo morpholinos resulted in loss of Purkinje cells (Kawahara and Hayashi, 2016). Hence, a profound role of SIL1 in neuronal function and maintenance can be postulated. This assumption is also supported by the crucial role of (functional) BiP levels for motor neuron survival (Penas et al., 2011) and observations that SIL1 elevation (i) attenuates motor neuron vulnerability in a mouse model of ALS (Filézac de L'Etang et al., 2015) and (ii) triggers the expression of proteins with neuroprotective properties (Labisch et al., 2017). To address the vulnerability of the PNS against SIL1 loss, we performed combined electron microscopic, immunofluorescence, proteomic and selected transcript studies. Results of our ultra-morphological studies on intra-muscular nerve fascicles from two MSS-patients and three woozy and wildtype mice revealed affection of myelinating and non-myelinating Schwann cells as

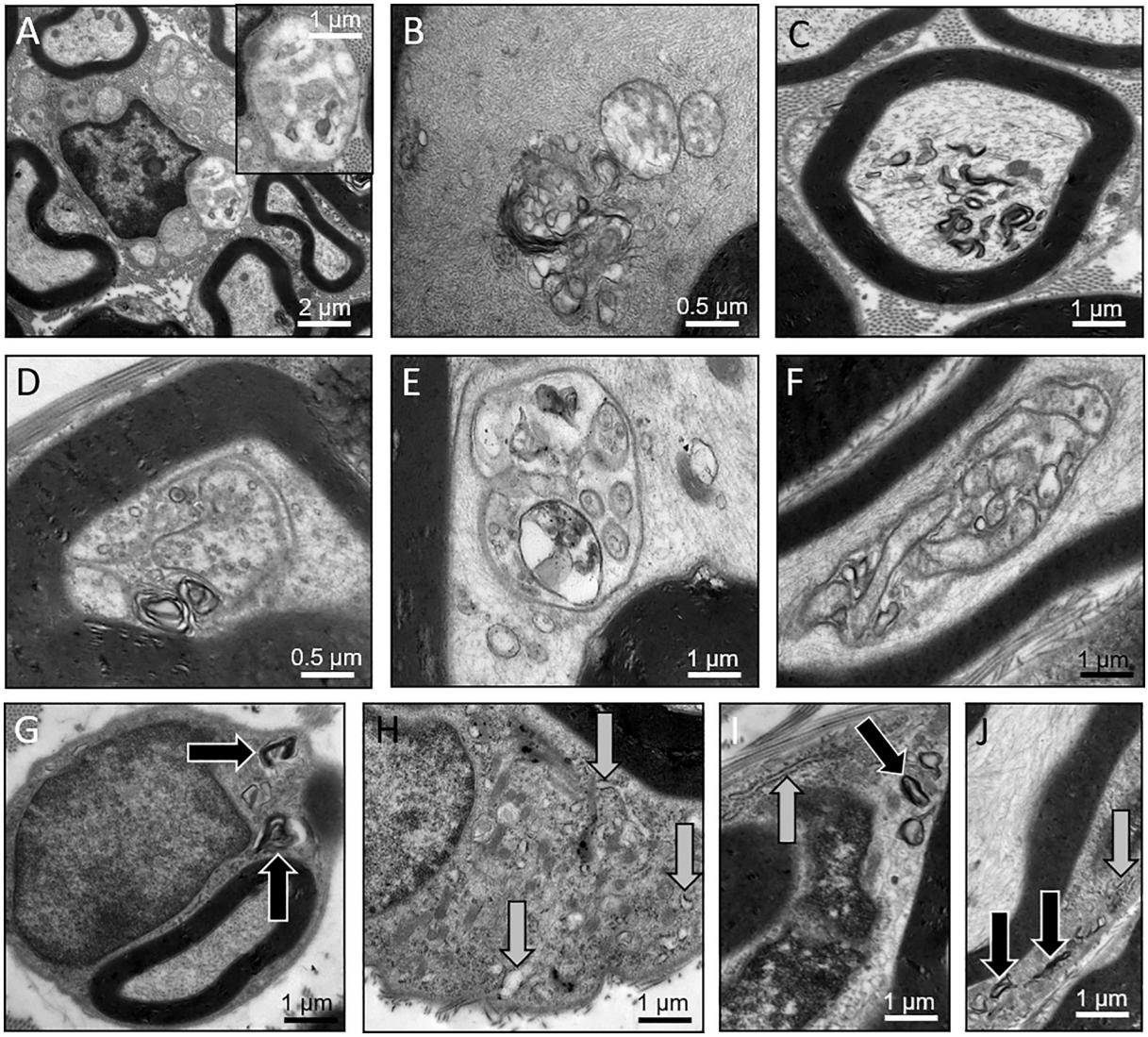

Fig. 4. Ultrastructural findings in sciatic nerves of 26-week-old woozy mice. (A) and inset in (A) degenerating unmyelinated axon in Remak bundle. (B, C) Accumulations of autophagic material in axons of myelinated nerve fibres. (D, E, F) Invaginations of the axolemma associated with accumulated autophagic material within the axons and in the adaxonal Schwann cell cytoplasm. (G) Autophagic vacuoles containing membranous material in the cytoplasm of a Schwann cell of a myelinated nerve fibre (black arrows). (H–J) Prominent ER structures (grey arrows) merging with membranous autophagic material (black arrows) in the cytoplasm of Schwann cells.

well as of axons engulfed by both types of Schwann cells. Hereby, changes in the architecture of the nuclear envelope were observed accompanied by mitochondrial degeneration and aggregates of autophagic material. These aggregates were remarkably prominent in myelinated axons of *Sil1*-mutant mice and were found to be more pronounced in 26- compared to 16-week-old animals. Interestingly, abnormal aggregates of autophagic material and perturbations of nuclear envelope structures as well as mitochondrial degeneration have already been extensively described in MSS-patient and *woozy* mouse muscle as well as in *in vitro* models of the disease (Roos et al., 2014; Roos et al., 2016) suggesting that these ultra-morphological changes are a consistent feature in tissues vulnerable for SIL1 loss. Moreover, this finding is in line with the results of a study linking levels of functional BiP to the activation of autophagy as a mechanism acting towards the breakdown of protein aggregates and to axonal degeneration (Penas et al., 2011).

The major differential diagnosis of MSS is the congenital cataracts, facial dysmorphism and peripheral neuropathy (CCFDN) syndrome due to a recurrent recessive mutation in *CTDP1*. CCFDN is associated with a symmetric, distal peripheral neuropathy with a predominant motor phenotype. Secondary scoliosis and foot deformities are common. Sensory neuropathy develops after age ten years (Kalaydjieva, 2006). Interestingly, scoliosis has also been described in 61% of patients with *SIL1* mutations (Roos et al., 2012). Our present findings suggest that MSS is phenotypically even more reminiscent to CCFDN, as neuropathy appears to be a consistent feature of SIL1 mutation in patients and mice. However, the buildup of autophagic material in MSS and *woozy* mice was present predominantly in axons, whereas the neuropathy in CCFDN was described to be hypo/demyelinating (Kalaydjieva, 2006). Moreover, myelination also seemed to be normal in the MSS-zebrafish model.

4.2. NMJs are vulnerable to the loss of SIL1

Axonal neuropathies often go along with defects of neuromuscular junctions (NMJs) (Spaulding et al., 2016). Therefore, we sought to determine whether perturbed NMJ integrity is a pathophysiological aspect of SIL1 deficiency. Immunofluorescence of NMJs in *woozy* mice revealed smaller NMJs and weaker fluorescence intensity for α-bungarotoxin, suggesting reduced presence of acetylcholine receptor

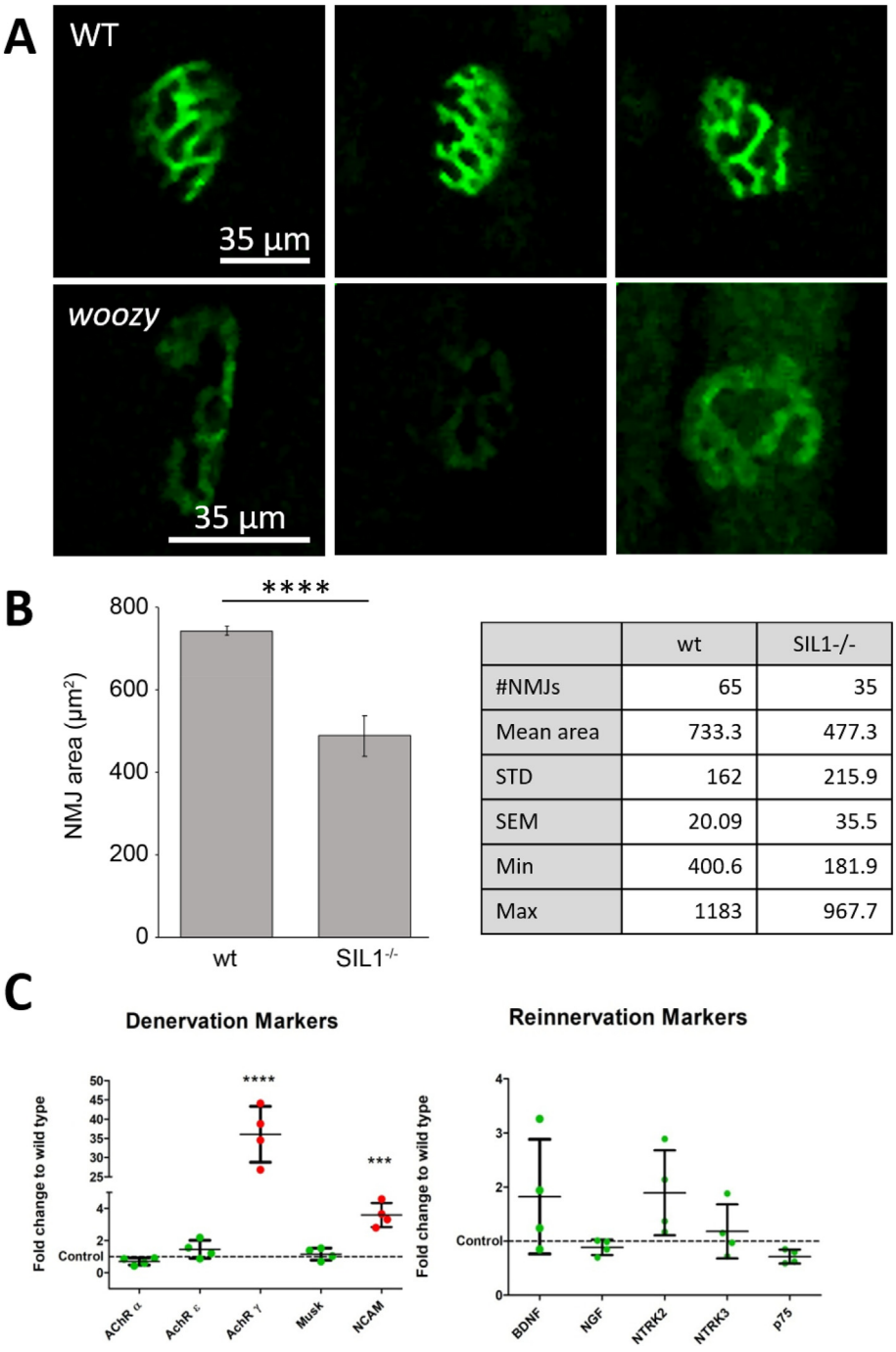

	wt	SIL1-/-
#NMJs	65	35
Mean area	733.3	477.3
STD	162	215.9
SEM	20.09	35.5
Min	400.6	181.9
Max	1183	967.7

Fig. 5. NMJ-analysis of Sil1-mutant and wild-type mice (26 weeks of age). (A) Visualization of NMJs via fluorescence-dye conjugated α-bungarotoxin binding to acetelycholine receptors revealed an overall reduced fluorescence intensity in the mutant animals compared to control suggesting reduced level of the receptor upon SIL1-deficiency. (B) Analysis of the size of wildtype and SIL1-mutant NMJs. (C) Studies of abundances of transcripts encoding for de-innervation (AChRα, AChRε, AChRγ, Musk, NCAM) and re-innervation markers (BDNF, NGF, NTRK2, NTRK3, p75) revealed significantly increased abundances of AChRγ and NCAM transcripts in Sil1-mutant animals compared to wildtype littermate controls. AChR = acetelycholine receptors; Musk = muscle, skeletal receptor tyrosine-protein kinase; NCAM = neural cell adhesion molecule; brain-derived neurotrophic factor; NGF = β-nerve growth factor; NTRK = high affinity nerve growth factor receptor; p75 = low affinity neurotrophin receptor p75NTR.

(AChR) subunits. Immunofluorescence of our MSS zebrafish model confirmed impaired NMJ integrity, supporting our findings obtained in *woozy* mice and demonstrating that this pathophysiological feature manifests across different species. Alterations of AChR density might, at least partially, result from a disturbed SIL1-BiP machinery involved in the folding of muscle membrane proteins such as AChRs. In this context, it is important to note that agrin which is secreted by axon endings and crucial for clustering of AChRs is also itself a substrate of a neuronal SIL1-BiP machinery. Our findings confirm our previous report of perturbed NMJ integrity in *woozy* mice (Filézac de L'Etang et al., 2015), and indicate that impairment of neuromuscular transmission is part of MSS pathophysiology. The concept of a pre- and post-synaptic impact is supported by results of our proteomic studies (discussed below in more detail) showing that gephyrin, a synapse/NMJ-associated protein (Mann and Kröger, 1996) is affected by Sil1-muation in murine sciatic nerves and by results of our targeted skeletal muscle transcript studies showing that NCAM as well as AChRγ display altered transcript abundances. Neural cell adhesion molecule (NCAM) plays a crucial role in the development and maturation of NMJs and is required for stability of re-innervated NMJs also by acting as a signal for regenerating axons (Covault and Sanes, 1985). Thus, the *NCAM* increase most likely is a compensatory mechanism preventing NMJs from complete breakdown in MSS. The strong increase of *AChRγ* transcript levels might also compensate for decreased AChR presence at the NMJs.

4.3. Proteomic changes in sciatic nerves of woozy mice allow molecular insights into PNS vulnerability

To obtain biochemical insights into PNS vulnerability upon SIL1-loss, comparative proteome profiling *via* a label-free approach was

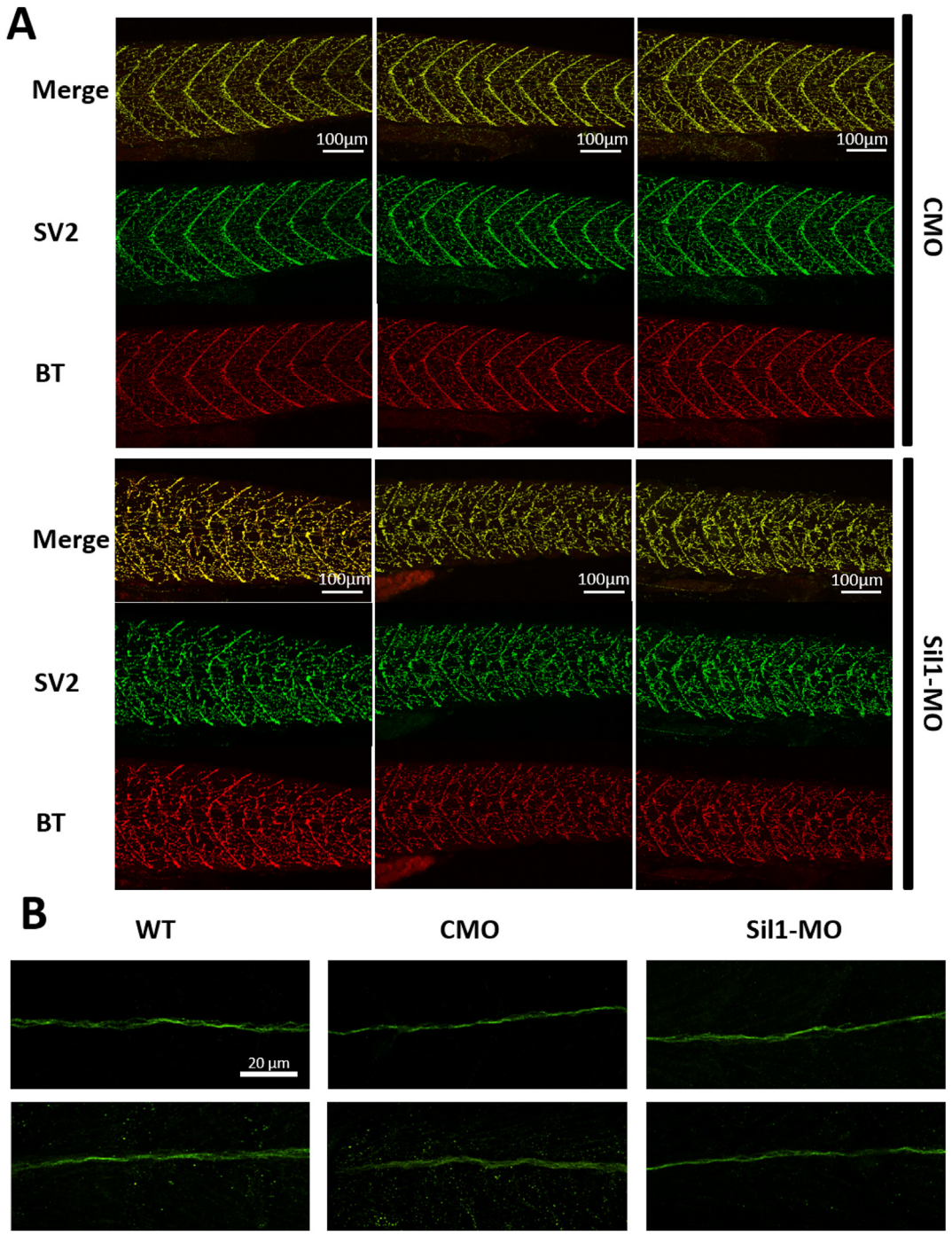

Fig. 6. Immunofluorescence studies in 48 hpf MSS-zebrafish. (A) Immunofluorescent studies of NMJs in control-MO (6A) & Sil1-MO (6B) injected embryos (6 ng of MO-injection respectively). SV2 stains presynaptic motor neurons and α-bungarotoxin detects the postsynaptic AChRs. Sil1-MO injected fish display disorganised branching of nerves and of synapses along the vertical myosepta. MO = morpholino, hpf = hours post fertilization, AChRs = acetelycholine receptors, SV2 = synaptic vesicle protein 2. (B) Staining of myelinating Schwann cells utilizing an anti-Claudin K antibody did not show significant differences between wildtype, control-morpholino (CMO) and Sil1-morpholino-injected fish (6C). Scale bar = 20 µm.

performed. To this end, the proteomic signature of SIL1-deficient sciatic nerve was examined utilizing three biological replicates derived from woozy and wildtype animals aged 26 weeks. Some of the proteins found to be affected prominently such as perilipin are major regulators of lipid homeostasis which is important for mitochondrial integrity and function (Aufschnaiter et al., 2017; Dettlaff-Pokora et al., 2016; Pourteymour et al., 2015; Chen et al., 2013). Pyruvate carboxylase (PYC) is a mitochondrial protein catalyzing ATP-dependent carboxylation. As fatty acid oxidation can be attenuated by PYC-inhibition, a decrease in SIL1-mutant nerves most likely serves as a protective mechanism. However, vulnerability of PYC activity in both non-synaptic and synaptic mitochondria against cellular stress burden has been demonstrated (Faff-Michalak and Albrecht, 1991) suggesting that decreased abundance of PYC in SIL1-mutant nerve might correspond with mitochondrial perturbations on the morphological level as well as with impaired function of the NMJs discussed above.

Mitochondrial defects promote ROS production (Lee et al., 2013), a fact which is in line with the detected increase in antioxidant factors

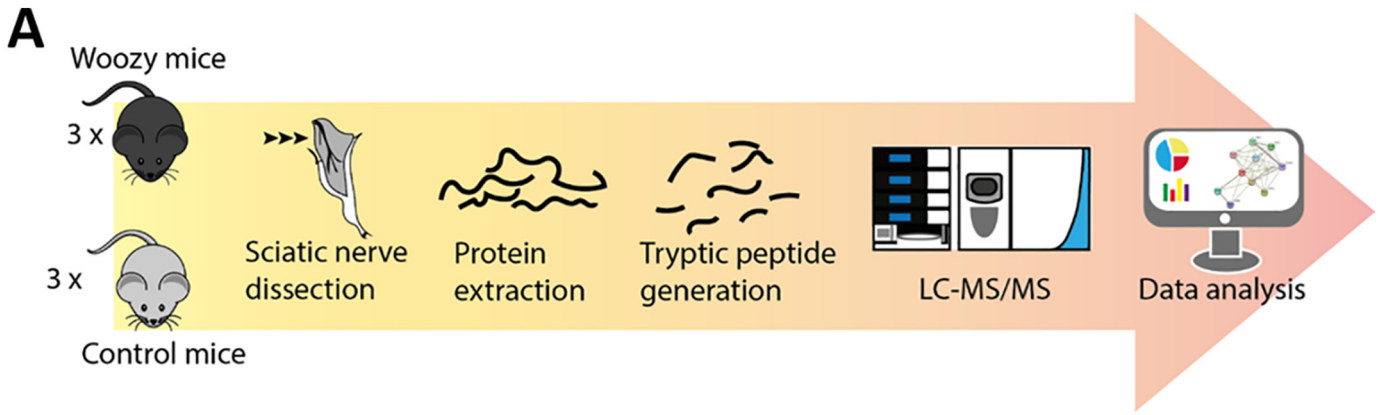

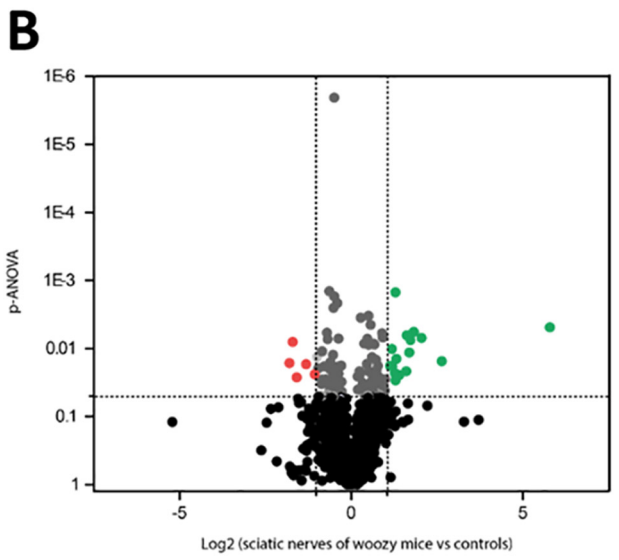

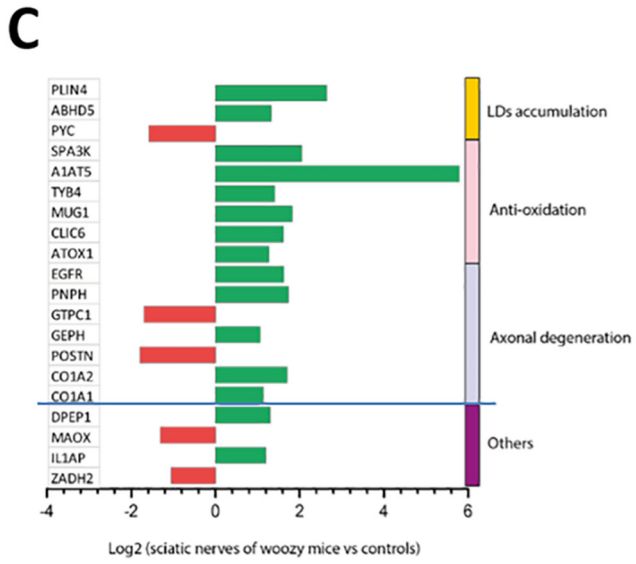

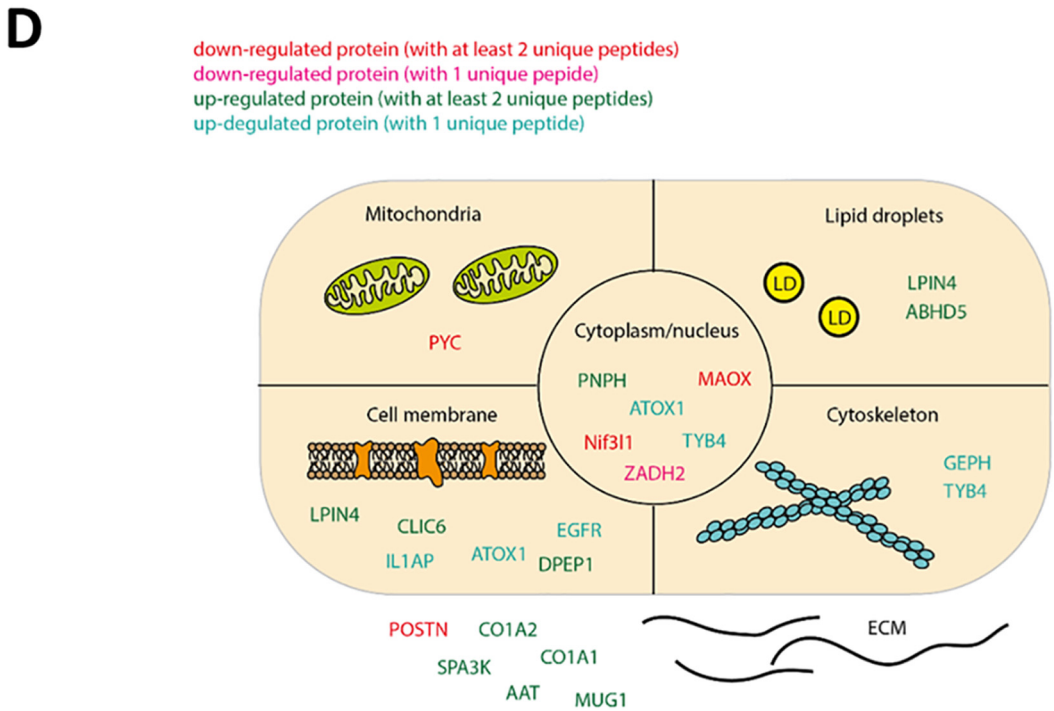

Fig. 7. Proteomic profiling of Sil1-mutant nerves. (A) Applied workflow. (B) Volcano plot of obtained proteomic results. (C) Diagram presenting the fold of protein-dysregulation and the function of the affected proteins. (D) Schematic presentation of the subcellular localization of the proteins altered in abundances upon the loss of functional SIL1 in murine sciatic nerves.

upon SIL1 deficiency, exemplified by the up-regulation of Murinoglobulin-1 (MUG1), Serine protease inhibitor A3K (SA3K), Chloride intracellular channel protein 6 (CLIC6), Alpha-1-antitrypsin 1–5 (A1AT5), Thymosin beta-4 (TYB4) and Copper transport protein ATOX1 (Griffon et al., 2003; Hatori and Lutsenko, 2016; Zhou et al., 2012). Interestingly, TYB4 improves neurological functional outcome and axonal remodeling after embolic stroke in rats also suggesting a neuroprotective function of this protein (Morris et al., 2010). EGFR promotes intrinsic axonal regeneration (Xu et al., 2014). Similarly, as purine nucleoside phosphorylase (PNPH) deficiency results in a disorder characterized by recurrent infections, neurologic symptoms (rigid muscles, ataxia, developmental delay, and intellectual disability) (Simmonds et al., 1987; Tam Jr. and Leshner, 1995), its increased abundance in *Sil1*-mutant PNS may also be a protective mechanism. Collagen nerve guides support axonal regeneration of the peripheral nerve (van Neerven et al., 2017) and COL1A1 and COL1A2 have been identified with increased abundance in woozy nerves. Gephyrin is well known to promote nerve survival by establishing synaptic specificity at the NMJs (Betz, 1998). Periostin (POSTN) has been identified to play a key role in axonal regeneration (Shih et al., 2014). Additionally, secreted POSTN has been shown to promote nerve regeneration in patients with peripheral neuropathies (Sonnenberg-Riethmacher et al., 2015). Therefore, the down-regulation of POSTN in the global profile either hints for an increasing activity of secreted POSTN in the extracellular space in axonal regeneration or contributes to axonal vulnerability. However, increased abundance of proteins with protective potential does not only indicate a vulnerability of the PNS against loss of functional SIL1, but also might explain why PNS pathology is subtle compared to cerebellar and skeletal muscle phenotype. In this context, it is worth noting that recently one of our molecular studies on organ vulnerability in MSS suggested that the presence of antagonizing factors modifies the vulnerability of cells/tissues against loss of functional SIL1 (Kollipara et al., 2017).

5. Conclusion

Results of our combined morphological and biochemical studies suggest that the PNS along with the NMJs are vulnerable to SIL1-deficiency in human, mouse, and zebrafish. Only few nerve fibres showed disproportionately thin myelin sheaths. In contrast, axonal mitochondria seem to be affected by the loss of SIL1, and the build-up of autophagic material in axons is progressive. Up-regulation of proteins supporting axonal survival not only support the concept of PNS vulnerability to SIL1-loss but might also explain why other cellular populations are more vulnerable. Moreover, our findings highlight that the presence of PNS pathology might be added to the spectrum of MSS and should be considered when delineating MSS from CCFDN in the clinical setting.

Ethics approval and consent to participate

Work with human MSS-samples (originally collected for diagnostic purposes) for further research studies has been approved by the ethical review committee of the University Hospital of RWTH-Aachen University (EK104/10). Work with woozy and wildtype mice was reviewed and approved by the Animal Care Committee of the University of Aachen (RWTH-Aachen). All mice were handled according to the guidelines from the Federation for European Laboratory Animal Science Association (FELASA).

Consent for publication

Not applicable.

Availability of data and material

The mass spectrometry proteomics data have been deposited to the ProteomeXchange Consortium *via* the PRIDE partner repository with the dataset identifier PXD009022.

Competing interests

The authors declare that they do not have any competing interests.

Funding

This work was supported by a grant from the START program of RWTH Aachen University (to A. R.; Grant No. 41/12), the French Muscular Dystrophy Association (AFM-Téléthon; #21644; grant to A.R.) and EU Joint Program Neurodegenerative Diseases (JPND), the German Federal Ministry of Education and Research (BMBF; CMT-Net 01GM1511D) and the DGM (MND-Net) to J.W. Financial support by the Ministerium für Innovation, Wissenschaft und Forschung des Landes Nordrhein-Westfalen, the Senatsverwaltung für Wirtschaft, Technologie und Forschung des Landes Berlin and the Bundesministerium für Bildung und Forschung is gratefully acknowledged.

Authors' contributions

A.R., R.H., H.L. and J.W. designed the study. Proteomic profiling was carried out by V.P. and A.R. and transcript studies have been performed by S.C. and S.S.; Animals were prepared by S.B. and T.S. and studies on murine NMJs were carried out by T.S. E.O. and R.R.; zebrafish models were generated and analyzed by D.H. and D.C.; H.H.G. provided images of intramuscular nerve fibres of the MSS-patients and electron microscopic studies of murine muscle and nerve samples have been carried out by A.R. and J.W.

Acknowledgements

We thank Hannelore Mader and Claudia Krude for expert technical assistance.

Appendix A. Supplementary data

Supplementary data to this article can be found online at https://doi.org/10.1016/j.nbd.2018.11.019.

References

Aare, S., Spendiff, S., Vuda, M., Elkrief, D., Perez, A., Wu, Q., Mayaki, D., Hussain, S.N.A., Hettwer, S., Hepple, R.T., 2016. Failed reinnervation in aging skeletal muscle. Skelet. Muscle 6, 29.

Anttonen, A.K., Mahjneh, I., Hamalainen, R.H., Lagier-Tourenne, C., Kopra, O., Waris, L., Anttonen, M., Joensuu, T., Kalimo, H., Paetau, A., et al., 2005. The gene disrupted in Marinesco-Sjogren syndrome encodes SIL1, an HSPA5 cochaperone. Nat. Genet. 37, 1309–1311.

Aufschnaiter, A., Kohler, V., Diessl, J., Peselj, C., Carmona-Gutierrez, D., Keller, W., Büttner, S., 2017. Mitochondrial lipids in neurodegeneration. Cell Tissue Res. 367, 125–140.

Betz, H., 1998. Gephyrin, a major player in GABAergic postsynaptic membrane assembly? Nat. Neurosci. 1, 541.

Burkhart, J.M., Gambaryan, S., Watson, S.P., Jurk, K., Walter, U., Sickmann, A., Heemskerk, J.W.M., Zahedi, R.P., 2014. What can proteomics tell us about platelets? Circ. Res. 114, 1204–1219.

Byrne, S., Dlamini, N., Lumsden, D., Pitt, M., Zaharieva, I., Muntoni, F., King, A., Robert, L., Jungbluth, H., 2015. SIL1-related Marinesco-Sjoegren syndrome (MSS) with associated motor neuronopathy and bradykinetic movement disorder. Neuromuscul. Disord. 25, 585–588.

Chen, W., Chang, B., Wu, X., Li, L., Sleeman, M., Chan, L., 2013. Inactivation of Plin4 downregulates Plin5 and reduces cardiac lipid accumulation in mice. Am. J. Physiol. Endocrinol. Metab. 304, E770–E779.

Chung, K.T., Shen, Y., Hendershot, L.M., 2002. BAP, a mammalian BiP-associated protein, is a nucleotide exchange factor that regulates the ATPase activity of BiP. J. Biol. Chem. 277, 47557–47563.

Covault, J., Sanes, J.R., 1985. Neural cell adhesion molecule (N-CAM) accumulates in denervated and paralyzed skeletal muscles. Proc. Natl. Acad. Sci. U. S. A. 82, 4544–4548.
Dettlaff-Pokora, A., Sledzinski, T., Swierczynski, J., 2016. Upregulation of Pnpla2 and Abhd5 and downregulation of G0s2 gene expression in mesenteric white adipose tissue as a potential reason for elevated concentration of circulating NEFA after removal of retroperitoneal, epididymal, and inguinal adipose tissue. Mol. Cell. Biochem. 422, 21–29.
Doyle, K.M., Kennedy, D., Gorman, A.M., Gupta, S., Healy, S.J., Samali, A., 2011. Unfolded proteins and endoplasmic reticulum stress in neurodegenerative disorders. J. Cell. Mol. Med. 15, 2025–2039.
Faff-Michalak, L., Albrecht, J., 1991. Aspartate aminotransferase, malate dehydrogenase, and pyruvate carboxylase activities in rat cerebral synaptic and nonsynaptic mitochondria: effects of in vitro treatment with ammonia, hyperammonemia and hepatic encephalopathy. Metab. Brain Dis. 6, 187–197.
Filézac de L'Etang, A., Maharjan, N., Cordeiro Braña, M., Ruegsegger, C., Rehmann, R., Goswami, A., Roos, A., Troost, D., Schneider, B.L., Weis, J., Saxena, S., 2015. Marinesco-Sjögren syndrome protein SIL1 regulates motor neuron subtype-selective ER stress in ALS. Nat. Neurosci. 18, 227.
Franceschini, A., Szklarczyk, D., Frankild, S., Kuhn, M., Simonovic, M., Roth, A., Lin, J., Minguez, P., Bork, P., von Mering, C., Jensen, L.J., 2013. STRING v9.1: protein-protein interaction networks, with increased coverage and integration. Nucleic Acids Res. 41, D808–D815.
Gai, N., Jiang, C., Zou, Y.-Y., Zheng, Y., Liang, D.-S., Wu, L.-Q., 2016. Novel SIL1 nonstop mutation in a Chinese consanguineous family with Marinesco-Sjögren syndrome and Dandy-Walker syndrome. Clin. Chim. Acta 458, 1–4.
Goto, M., Okada, M., Komaki, H., Sugai, K., Sasaki, M., Noguchi, S., Nonaka, I., Nishino, I., Hayashi, Y.K., 2014. A nationwide survey on Marinesco-Sjogren syndrome in Japan. Orphanet J. Rare Dis. 9, 58.
Griffon, N., Jeanneteau, F., Prieur, F., Diaz, J., Sokoloff, P., 2003. CLIC6, a member of the intracellular chloride channel family, interacts with dopamine D(2)-like receptors. Brain Res. Mol. Brain Res. 117, 47–57.
Hatori, Y., Lutsenko, S., 2016. The role of copper chaperone Atox1 in coupling redox homeostasis to intracellular copper distribution. Antioxidants (Basel) 5.
Herva, R., von Wendt, L., von Wendt, G., Saukkonen, A.L., Leisti, J., Dubowitz, V., 1987. A syndrome with juvenile cataract, cerebellar atrophy, mental retardation and myopathy. Neuropediatrics 18, 164–169.
Horvers, M., Anttonen, A.K., Lehesjoki, A.E., Morava, E., Wortmann, S., Vermeer, S., van de Warrenburg, B.P., Willemsen, M.A., 2013. Marinesco-Sjögren syndrome due to SIL1 mutations with a comment on the clinical phenotype. Eur. J. Paediatr. Neurol. 17, 199–203.
Inaguma, Y., Hamada, N., Tabata, H., Iwamoto, I., Mizuno, M., Nishimura, Y.V., Ito, H., Morishita, R., Suzuki, M., Ohno, K., et al., 2014. SIL1, a causative cochaperone gene of Marinesco-Sojgren syndrome, plays an essential role in establishing the architecture of the developing cerebral cortex. EMBO Mol. Med. 6, 414–429.
Kalaydjieva, L., 2006. Congenital cataracts – facial dysmorphism – neuropathy. Orphanet J. Rare Dis. 1, 32.
Kawahara, G., Hayashi, Y.K., 2016. Characterization of zebrafish models of Marinesco-Sjögren syndrome. PLoS One 11, e0165563.
Khan, M.M., Lustrino, D., Silveira, W.A., Wild, F., Straka, T., Issop, Y., O'Connor, E., Cox, D., Reischl, M., Marquardt, T., et al., 2016. Sympathetic innervation controls homeostasis of neuromuscular junctions in health and disease. Proc. Natl. Acad. Sci. U. S. A. 113, 746–750.
Kimmel, C.B., Ballard, W.W., Kimmel, S.R., Ullmann, B., Schilling, T.F., 1995. Stages of embryonic development of the zebrafish. Dev. Dyn. 203, 253–310.
Kollipara, L., Buchkremer, S., Coraspe, J.A.G., Hathazi, D., Senderek, J., Weis, J., Zahedi, R.P., Roos, A., 2017. In-depth phenotyping of lymphoblastoid cells suggests selective cellular vulnerability in Marinesco-Sjogren syndrome. Oncotarget 8, 68493–68516.
Krieger, M., Roos, A., Stendel, C., Claeys, K.G., Sonmez, F.M., Baudis, M., Bauer, P., Bornemann, A., de Goede, C., Dufke, A., et al., 2013. SIL1 mutations and clinical spectrum in patients with Marinesco-Sjogren syndrome. Brain 136, 3634–3644.
Labisch, T., Buchkremer, S., Phan, V., Kollipara, L., Gatz, C., Lentz, C., Nolte, K., Vervoorts, J., Coraspe, J.A., Sickmann, A., et al., 2018. Tracking effects of SIL1 increase: taking a closer look beyond the consequences of elevated expression level. Mol. Neurobiol. 55 (3), 2524–2546. https://doi.org/10.1007/s12035-017-0494-6. Epub 2017 Apr 11.
Lee, S.-J., Zhang, J., Choi, A.M.K., Kim, H.P., 2013. Mitochondrial dysfunction induces formation of lipid droplets as a generalized response to stress. Oxidative Med. Cell. Longev. 2013, 327167.
Liu, Z.C., Chu, J., Lin, L., Song, J., Ning, L.N., Luo, H.B., Yang, S.S., Shi, Y., Wang, Q., Qu, N., et al., 2016. SIL1 rescued Bip elevation-related tau hyperphosphorylation in ER stress. Mol. Neurobiol. 53, 983–994.
Mann, S., Kröger, S., 1996. Agrin is synthesized by retinal cells and colocalizes with gephyrin. corrected title. Mol. Cell. Neurosci. 8, 1–13.
Morris, D.C., Chopp, M., Zhang, L., Lu, M., Zhang, Z.G., 2010. Thymosin beta4 improves functional neurological outcome in a rat model of embolic stroke. Neuroscience 169, 674–682.
Müller, J.S., Jepson, C.D., Laval, S.H., Bushby, K., Straub, V., Lochmüller, H., 2010. Dok-7 promotes slow muscle integrity as well as neuromuscular junction formation in a zebrafish model of congenital myasthenic syndromes. Hum. Mol. Genet. 19, 1726–1740.
van Neerven, S.G.A., Haastert-Talini, K., Boecker, A., Schriever, T., Dabhi, C., Claeys, K., Deumens, R., Brook, G.A., Weis, J., Pallua, N., Bozkurt, A., 2017. Two-component collagen nerve guides support axonal regeneration in the rat peripheral nerve injury model. J. Tissue Eng. Regen. Med. 11, 3349–3361.
Noreau, A., La Piana, R., Marcoux, C., Canada, F., Dion, P.A., Brais, B., Bernard, G., Rouleau, G.A., 2015. Novel SIL1 mutations cause cerebellar ataxia and atrophy in a French-Canadian family. Neurogenetics 16, 315–318.
Penas, C., Font-Nieves, M., Forés, J., Petegnief, V., Planas, A., Navarro, X., Casas, C., 2011. Autophagy, and BiP level decrease are early key events in retrograde degeneration of motoneurons. Cell Death Differ. 18, 1617.
Pourteymour, S., Lee, S., Langleite, T.M., Eckardt, K., Hjorth, M., Bindesboll, C., Dalen, K.T., Birkeland, K.I., Drevon, C.A., Holen, T., Norheim, F., 2015. Perilipin 4 in human skeletal muscle: localization and effect of physical activity. Phys. Rep. 3.
Roos, A., Schwanitz, G., Diepolder, I., Senderek, J., Eggermann, K., 2012. Search for Cryptic Subtelomeric Aberrations in Patients With Non-classical Marinesco-Sjögren Phenotype.
Roos, A., Buchkremer, S., Kollipara, L., Labisch, T., Gatz, C., Zitzelsberger, M., Brauers, E., Nolte, K., Schroder, J.M., Kirschner, J., et al., 2014. Myopathy in Marinesco-Sjogren syndrome links endoplasmic reticulum chaperone dysfunction to nuclear envelope pathology. Acta Neuropathol. 127, 761–777.
Roos, A., Kollipara, L., Buchkremer, S., Labisch, T., Brauers, E., Gatz, C., Lentz, C., Gerardo-Nava, J., Weis, J., Zahedi, R.P., 2016. Cellular signature of SIL1 depletion: disease pathogenesis due to alterations in protein composition beyond the ER machinery. Mol. Neurobiol. 53, 5527–5541.
Roos A, Thompson R, Horvath R, Lochmüller H, Sickmann A. Intersection of proteomics and genomics to "solve the unsolved" in rare disorders such as neurodegenerative and neuromuscular diseases. Proteomics Clin. Appl. 1700073-n/a.
Roy, S., Johnston, A.H., Newman, T.A., Glueckert, R., Dudas, J., Bitsche, M., Corbacella, E., Rieger, G., Martini, A., Schrott-Fischer, A., 2010. Cell-specific targeting in the mouse inner ear using nanoparticles conjugated with a neurotrophin-derived peptide ligand: potential tool for drug delivery. Int. J. Pharm. 390, 214–224.
Schlosser, A., Volkmer, R., 2003. Volatile Polydimethylcyclosiloxanes in the Ambient Laboratory Air Identified as Source of Extreme Background Signals in Nanoelectrospray Mass Spectrometry.
Senderek, J., Krieger, M., Stendel, C., Bergmann, C., Moser, M., Breitbach-Faller, N., Rudnik-Schoneborn, S., Blaschek, A., Wolf, N.I., Harting, I., et al., 2005. Mutations in SIL1 cause Marinesco-Sjogren syndrome, a cerebellar ataxia with cataract and myopathy. Nat. Genet. 37, 1312–1314.
Shih, C.H., Lacagnina, M., Leuer-Bisciotti, K., Proschel, C., 2014. Astroglial-derived periostin promotes axonal regeneration after spinal cord injury. J. Neurosci. 34, 2438–2443.
Simmonds, H.A., Fairbanks, L.D., Morris, G.S., Morgan, G., Watson, A.R., Timms, P., Singh, B., 1987. Central nervous system dysfunction and erythrocyte guanosine triphosphate depletion in purine nucleoside phosphorylase deficiency. Arch. Dis. Child. 62, 385–391.
Sjogren, T., 1950. Hereditary congenital spinocerebellar ataxia accompanied by congenital cataract and oligophrenia; a genetic and clinical investigation. Confin. Neurol. 10, 293–308.
Sonnenberg-Riethmacher, E., Miehe, M., Riethmacher, D., 2015. Promotion of periostin expression contributes to the migration of Schwann cells. J. Cell Sci. 128, 3345–3355.
Spaulding, E.L., Sleigh, J.N., Morelli, K.H., Pinter, M.J., Burgess, R.W., Seburn, K.L., 2016. Synaptic deficits at neuromuscular junctions in two mouse models of Charcot–Marie–tooth type 2d. J. Neurosci. 36, 3254–3267.
Stetler, R.A., Gan, Y., Zhang, W., Liou, A.K., Gao, Y., Cao, G., Chen, J., 2010. Heat shock proteins: cellular and molecular mechanisms in the central nervous system. Prog. Neurobiol. 92, 184–211.
Superneau, D.W., Wertelecki, W., Zellweger, H., Bastian, F., 1987. Myopathy in Marinesco-Sjogren syndrome. Eur. Neurol. 26, 8–16.
Tam Jr., D.A., Leshner, R.T., 1995. Stroke in purine nucleoside phosphorylase deficiency. Pediatr. Neurol. 12, 146–148.
Xu, M.F., Zhou, H., Hu, C.Y., Liang, Y.Q., Hu, L., Chen, D., 2014. The mechanisms of EGFR in the regulation of axon regeneration. Cell Biochem. Funct. 32, 101–105.
Zhao, L., Longo-Guess, C., Harris, B.S., Lee, J.-W., Ackerman, S.L., 2005. Protein accumulation and neurodegeneration in the woozy mutant mouse is caused by disruption of SIL1, a cochaperone of BiP. Nat. Genet. 37, 974.
Zhao, L., Rosales, C., Seburn, K., Ron, D., Ackerman, S.L., 2010. Alteration of the unfolded protein response modifies neurodegeneration in a mouse model of Marinesco-Sjogren syndrome. Hum. Mol. Genet. 19, 25–35.
Zhou, T., Zong, R., Zhang, Z., Zhu, C., Pan, F., Xiao, X., Liu, Z., He, H., Ma, J.X., Liu, Z., Zhou, Y., 2012. SERPINA3K protects against oxidative stress via modulating ROS generation/degradation and KEAP1-NRF2 pathway in the corneal epithelium. Invest. Ophthalmol. Vis. Sci. 53, 5033–5043.
Zoghbi, H.Y., 2005. SILencing misbehaving proteins. Nat. Genet. 37, 1302–1303.